Atomically Thin Nonlinear Transition Metal Dichalcogenide Holograms

Arindam Dasgupta, Jie Gao,* and Xiaodong Yang*

Department of Mechanical and Aerospace Engineering, Missouri University of Science and Technology, Rolla, Missouri 65409, United States

S *Supporting Information*

ABSTRACT: Nonlinear holography enables optical beam generation and holographic image reconstruction at new frequencies other than the excitation fundamental frequency, providing pathways toward unprecedented applications in optical information processing and data security. So far, plasmonic metasurfaces with the thickness of tens of nanometers have been mostly adopted for realizing nonlinear holograms with the potential of on-chip integration but suffering from low conversion efficiency and high absorption loss. Here, we report a nonlinear transition metal dichalcogenide (TMD) hologram with high conversion efficiency and atomic thickness made of only single nanopatterned tungsten disulfide (WS_2) monolayer, for producing optical vortex beams and Airy beams as well as reconstructing complex holographic images at the second harmonic (SH) frequency. Our concept of nonlinear TMD holograms paves the way toward not only the understanding of light−matter interactions at the atomic level but the integration of functional TMD-based devices with atomic thickness into the next-generation photonic circuits for optical communication, high-density optical data storage, and information security.

KEYWORDS: *Nonlinear holography, 2D materials, transition metal dichalcogenide monolayer, second-harmonic generation*
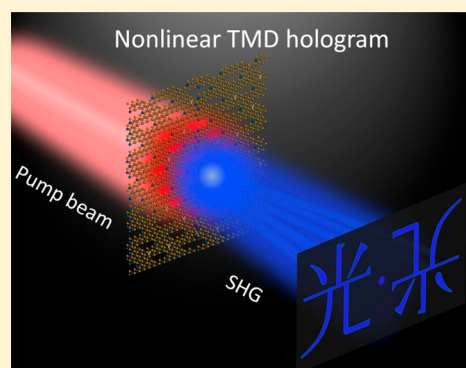
A hologram contains both the amplitude and phase information on the specified wavefront for generating the corresponding optical holographic image diffracted in the far field,[1] where light polarization, orbital angular momentum, and spatial intensity distribution can be precisely tailored and controlled. Hence, holography has become a promising approach for arbitrary beam shaping and predesigned image recording and reconstruction with a plethora of applications across many fields such as optical communication, optical tweezers,[2,3] data storage,[4,5] information security,[6] and three-dimensional displays.[3,7] Rather than linear holography, nonlinear holography introducing the converted frequencies as an extra degree of freedom has recently attracted great attention to meet the ever-increasing demands for high-density optical storage, optical information security, and biomedical imaging. Conventional nonlinear holographic devices have mainly used the modulated quadratic nonlinear optical materials such as ferroelectric crystals,[8] however, these bulky nonlinear crystals are incompatible with the on-chip photonic integration. The emergence of plasmonic metasurfaces has provided a significant breakthrough in bringing the nonlinear hologram thickness down to tens of nanometers.[9,10] Over the past few years, nonlinear metasurface holograms made of different types of plasmonic nanoantennas have been widely studied to produce optical beams and holographic images based on the nonlinear optical processes of second-harmonic generation (SHG),[11,12,13] third-harmonic generation (THG),[14,15] and

four-wave mixing.[16] Yet, nonlinear plasmonic metasurface holograms suffer from low conversion efficiency, high absorption loss, and small laser damage threshold which hinder their practical uses. More recently, dielectric THG metasurface holograms consisting of silicon resonators have been demonstrated to increase the nonlinear conversion efficiency by 2 orders of magnitude through the use of Mie resonances[17] but the thickness of these holograms is hundreds of nanometers which is unlikely to reach the deep subwavelength scale due to the nature of Mie scattering.

In that perspective, atomically thin TMD monolayers with high second-order nonlinear susceptibility ($\chi^{(2)}$) of few nm/V (several orders of magnitude higher than common nonlinear crystals)[18,19] have garnered a lot of interest in integrated nonlinear optics. Besides, negligible absorption loss and the capability for easy interfacing at the nanoscale[20] make TMD monolayer crystals ideal candidates for building on-chip nonlinear optical devices. Here, we experimentally demonstrate the concept of an atomically thin nonlinear TMD hologram with high conversion efficiency based on only single nano-patterned WS_2 monolayer. The WS_2 monolayer is patterned with the designed binary-amplitude computer-generated holo-gram (CGH) to encode the phase and amplitude of the desired

wavefront, and the corresponding SH optical image is diffracted at the Fourier plane in the far field. We demonstrate the nonlinear generation of optical vortex beams, two-dimensional (2D) Airy beams, and complex holographic images. Moreover, the polarization analysis is performed to show that the valley-contrasting physics associated with TMD monolayer provides deterministic control over the polarization state of the generated beam.

The calculated binary-amplitude CGH patterns are directly milled in the chemical vapor deposition grown WS$_2$ monolayer on c-cut sapphire substrate by using focused ion beam (FIB) (see Methods for details). Based on the Lee method,[21] the phase and amplitude of the desired wavefront at the CGH is encoded by the binary amplitude modulation[22] in $\chi^{(2)}$ of the WS$_2$ monolayer as

$$\chi_{\text{eff}}^{(2)}(x, y) = \chi^{(2)}\left(\frac{1}{2} + \frac{1}{2}\text{sign}\left\{\cos\left[\frac{2\pi x}{\Lambda} - \phi(x, y)\right]\right.\right.$$
$$\left.\left. - \cos[\sin^{-1} A(x, y)]\right\}\right) \quad (1)$$

where $\phi(x, y)$ and $A(x, y)$ are the phase and amplitude of the desired wavefront in the hologram plane, x and y are the spatial coordinates of the hologram plane, and Λ is the grating period for off-axis diffraction. By shinning the CGH with the fundamental wave E_{fund}, the SH emission at the hologram plane E_{SHG} will have the form of

$$E_{\text{SHG}}(x, y) \propto \chi_{\text{eff}}^{(2)}(x, y)E_{\text{fund}}(x, y)^2 \quad (2)$$

Hence, the target optical image will be reconstructed in the far field at the first diffraction order of $k_x = \pm\frac{2\pi}{\Lambda}$ with the diffraction angle given by the Raman-Nath relation[23]

$$\theta_{\text{SHG}} = \sin^{-1}\left(\frac{\lambda_{\text{SHG}}}{\Lambda}\right) \quad (3)$$

where λ_{SHG} is the SH wavelength.

First, the generation of SH vortex beam is demonstrated with the nonlinear TMD hologram. Vortex beams carrying orbital angular momentum (OAM) have been harnessed for numerous applications such as optical tweezers,[24,25] OAM photon qubits[26] and optical communications.[27] The electric field of a vortex beam can be represented in cylindrical coordinate by $E(r, \phi, z) = u(r, z)e^{-ikz}e^{il\phi}$, where **k** is the wavevector and l is the topological charge (TC) representing the OAM of $l\hbar$ per photon. In order to produce a vortex beam, the azimuthal phase profile in the hologram plane is

$$\phi(x, y) = \begin{cases} l\cdot\tan^{-1}\left(\frac{y}{x}\right) & x \geq 0 \\ l\cdot\left(\tan^{-1}\left(\frac{y}{x}\right) + \pi\right) & x < 0 \end{cases} \quad (4)$$

and the amplitude profile is $A(x, y) = 1$. Figure 1a is an optical transmission microscope image of the CGH patterned on a WS$_2$ monolayer triangle for producing the vortex beam with TC = 1. The fork hologram is designed in an area of 25 × 25 μm^2 with a grating period of $\Lambda = 3$ μm. Figure 1b,c shows the scanning electron microscope (SEM) image and SH image of the hologram, respectively. The dark parts in both the SEM and SH images indicate the areas where WS$_2$ is etched out during the FIB milling. A Fourier microscopy system is used to
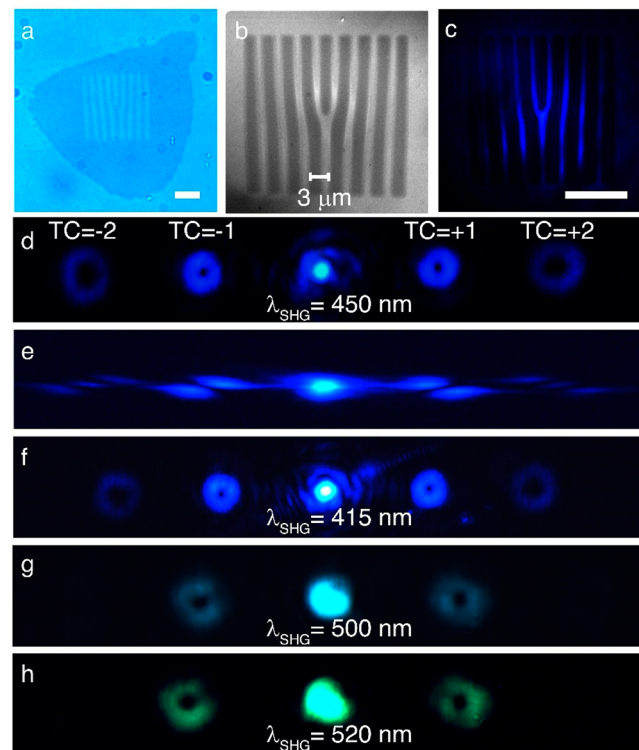

Figure 1. Generation of SH vortex with TC = 1. (a) Optical transmission microscope image and (b) SEM image of the CGH patterned on WS$_2$ monolayer triangle for producing SH vortex with TC = ±1. (c) SH image of the same hologram at SH wavelength (λ_{SHG}) of 450 nm. Scale bar is 10 μm. (d) Far-field image of the generated SH vortices at λ_{SHG} of 450 nm with the ±1-order diffraction angle θ_{SHG} of 8.6°. (e) Cylindrical lens converted image confirming that the TCs of SH vortices are indeed ±1 and ±2 at the ±1 and ±2 diffraction order, respectively. (f–h) Far-field images of the SH vortices at λ_{SHG} of 415, 500, and 520 nm, respectively.

characterize the generated beam profile in the far field (see Methods and Figure S1 of Supporting Information for the details of the system). The spot diameter of the Gaussian fundamental beam is set around 22 μm to make sure that most of the area of the hologram is illuminated, and the excitation power is set at 80 mW. In Figure 1d, the far-field image of the SH emission at the SH wavelength of 450 nm shows that the target vortex beams with the opposite TCs of ±1 are produced in the Fourier plane of the hologram at the ±1 diffraction order with the measured diffraction angle $\theta_{\text{SHG}} = 8.6°$. Two additional vortices with TC = ±2 and lower intensities are also observed at the ±2 diffraction order. The TC of each SH vortex is determined by performing an astigmatic transformation of the far field image using a cylindrical lens in front of the camera.[28] During the astigmatic transformation, the high-TC optical vortex splits into its constituent elementary vortices with unity TC to form an extended pattern of tilted dark stripes near the focal plane of the cylindrical lens. The count of the number of dark stripes indicates the TC and the stripe orientation determines the sign. The cylindrical lens-converted image in Figure 1e confirms the TC associated with each SH vortex. The broadband operation of the hologram is further demonstrated with the vortex generation at several SH wavelengths between 400 and 520 nm. Figure 1f–h shows the images of the generated vortices at the SH wavelengths of 415, 500, and 520 nm, respectively. θ_{SHG} gradually gets larger as the

SH wavelength increases, following the Raman-Nath relation of eq 3 (Figure S2 of Supporting Information). Apart from changing the wavelength, θ_{SHG} can also be varied by changing the grating period Λ, which is verified by fabricating another fork hologram with $\Lambda = 1.6$ μm giving $\theta_{SHG} = 16.2°$ at the SH wavelength of 450 nm (Figure S3 of Supporting Information).

The overall efficiency of the hologram η represents what fraction of the input fundamental power is converted into a particular SH vortex mode at the output, which is estimated by the product of the SH conversion efficiency (CE) (the ratio of total SH power and the fundamental beam power) and the diffraction efficiency (DE) (the fraction of the converted SH power coupled to a particular diffraction order), as $\eta = CE \cdot DE$. The evolution of CE and DE for each SH vortex as a function of SH wavelength is plotted in Figure 2 for an excitation laser
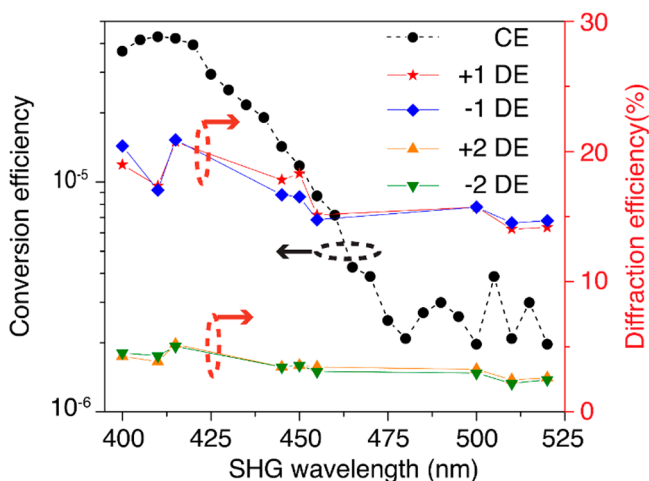

Figure 2. Evolution of the SHG CE from the hologram and the DE for different vortex diffraction orders as a function of SH wavelength. Excitation power is 80 mW which corresponds to a peak intensity of 21.1 kW·cm^{-2}.

power of 80 mW corresponding to the peak intensity of 21.1 kW·cm^{-2}. We observe that the SHG CE for the WS$_2$ monolayer hologram remains between 2×10^{-6} to 4×10^{-5} across a broad SH wavelength range of 400−520 nm, which is significantly higher than the previously achieved SHG CE in the order of 10^{-11} to 10^{-9} for plasmonic metasurfaces[9,11,12] and is in the same order of 10^{-5} observed in all-dielectric metasurfaces made of III−V semiconductors such as gallium arsenide[29] and aluminum gallium arsenide.[30] Moreover, the WS$_2$ monolayer possesses an atomic thickness of less than 1 nm, which is much thinner compared to the usual 30−50 nm thickness of plasmonic metasurfaces and several hundred nanometers thickness of all-dielectric metasurfaces. The measured DE for the ± 1 and ± 2-order vortices are in the range of 15−20% and 2.5−5%, respectively. At the SH wavelength of 450 nm, we determine that $\eta \approx 2 \times 10^{-6}$ for TC = ± 1 vortices and $\eta \approx 4 \times 10^{-7}$ for TC = ± 2 vortices.

Like other TMDs, WS$_2$ monolayer is a noncentrosymmetric hexagonal crystal with 3-fold rotational symmetry belonging to the D_{3h} symmetry group. Therefore, the intensity of SH emission from WS$_2$ monolayer strongly depends on the polarization state of the fundamental pump beam.[31−33] If we consider an arbitrary elliptical polarization for the excitation laser beam of $E = E_0(\cos \theta \hat{x} \pm i \sin \theta \hat{y})$ with θ being the ellipticity angle, the 3-fold rotational symmetry of WS$_2$ monolayer crystal induces the second-order polarization of the form $\mathbf{P}^{(2)} = \epsilon_0 \chi^{(2)} E_0^2 [\mp i \sin (2\theta)\hat{x} - \hat{y}]$ in the material.[33] Therefore, the resulting SHG signal is given by $I_{SHG} \propto (1 + \sin^2 2\theta)$ which suggests a 2-fold SHG intensity modulation as the incident polarization is changed from linear to circular polarization. To explore this effect on the SH vortex generation from the WS$_2$ hologram, the variations in the intensities of ± 1 and ± 2-order vortices as a function of the ellipticity of the fundamental excitation beam are monitored. We control the ellipticity of the fundamental beam by varying the angle (θ) between a linear polarizer (LP) fixed along the horizontal direction (0°) and the fast axis of a quarter-wave plate (QWP). Figure 3a,b plots the SH intensity variations for the +1, +2 and
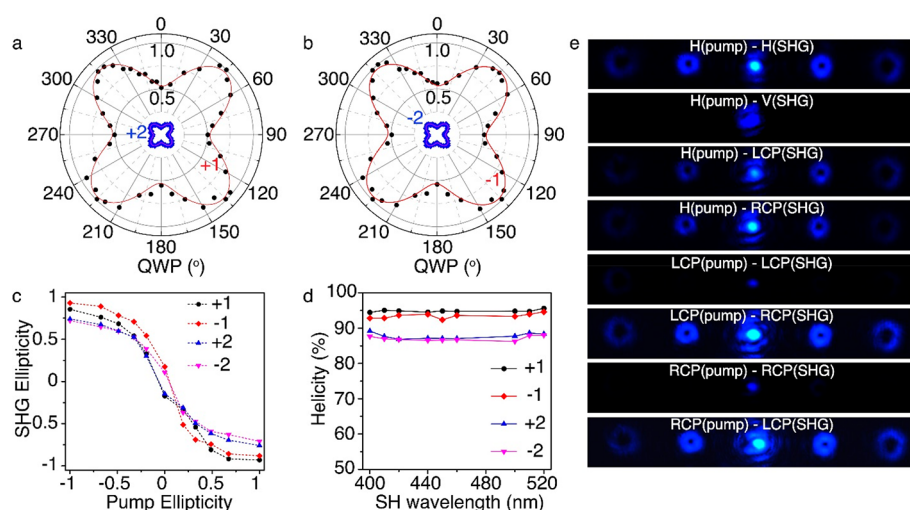

Figure 3. Dependence of the intensity and ellipticity of SH vortices on the polarization state of fundamental pump beam. Polar plots of the normalized SH intensity as a function of QWP angle for (a) the +1 and +2-order vortices, and (b) the −1 and −2-order vortices. (c) Evolution of the ellipticity of SH vortices as a function of the ellipticity of fundamental pump beam. (d) Helicity of all the SH vortices as a function of SH wavelength when the hologram is excited with RCP fundamental pump beam. (e) SH images for different combinations of the incident pump polarization and the output SH polarization, showing the polarization nonlinear selection rule. H and V represent horizontal and vertical linear polarization states, respectively.

−1, −2-order vortices as a function of the polarization state of the fundamental pump beam. For all the SH vortices, the observed four-lobe patterns suggest that the intensity of the SH signal for the circularly polarized excitation ($\theta = 45° + m\cdot90°$) is twice of that under the linearly polarized excitation ($\theta = 0° + m\cdot90°$). The ellipticity of the generated SH vortices is also monitored as a function of the ellipticity of fundamental beam by measuring the Stokes parameters (see Supporting Information S1). Figure 3c shows that the evolution of the ellipticity of SH vortices almost follows a sinusoidal dependence on that of fundamental beam where + and − sign indicates right- and left-handed elliptical polarization. The results indicate that linearly polarized excitation generates SH beams with almost the same polarization. However, an elliptically polarized excitation produces the spin-flipped SH vortices, manifesting the valley-contrasting physics of TMD monolayer. Because of the presence of strong spin−orbit coupling, TMD monolayer exhibits energy-degenerate valleys in the momentum space at the corners of the first Brillouin zone (K and K' points), composed of opposite spin states and thus can selectively absorb or emit the right- or left-handed circularly polarized (RCP or LCP) light. The previous studies indicate a spin flip in such polarization nonlinear selection rule for two-photon interband transition.[20,34] Thereby, during the SHG process, simultaneous absorption of two RCP (or LCP) fundamental photons at K (or K') leads to the emission of a counter-circularly polarized SH photon. Figure 3d plots helicity of all the SH vortices as a function of SH wavelength in the case of RCP excitation (see Figure S4 of Supporting Information for the corresponding case of LCP excitation). The helicity is defined as $H = \left(\frac{I(\text{RCP}) - I(\text{LCP})}{I(\text{RCP}) + I(\text{LCP})} \times 100\right)\%$ where $I(\text{RCP})$ and $I(\text{LCP})$ are the measured SH intensity of the RCP and LCP components. The measured H remains around −94% and −89% for the ±1 and ±2 diffraction order, respectively. The images of SH vortices in Figure 3e for a series of different combinations of the incident pump polarization and the output SH polarization state further justify the measured high helicity for the produced SH vortices and manifest the polarization nonlinear selection rule. We also demonstrate the crystal symmetry related intensity variations of the generated SH vortices at different diffraction orders as a function of the linear polarization angle of the fundamental pump beam in Figure S5 of Supporting Information (see Supporting Information S2).

The generation of SH vortices with TC = 2 and 3 is also demonstrated. Figure 4a,b shows the SEM image and SH image of the patterned hologram with $\Lambda = 1.6$ μm on WS$_2$ monolayer for producing the SH vortices of TC = 2. Figure 4c,e shows the images of SH vortices in the +1 and −1 diffraction order, whereas Figure 4d,f shows the corresponding cylindrical lens images confirming the TC to be +2 and −2, respectively. Figure 4g−l shows the experimental results for generating the SH vortices of TC = 3. Furthermore, the generation of 2D-Airy beam with nonlinear TMD hologram is explored, as the self-accelerating and self-healing Airy beams have important applications in optical manipulation[35] and microscopy.[36] To generate the CGH, the cubic phase of a 2D-Airy beam is encoded in the hologram plane by
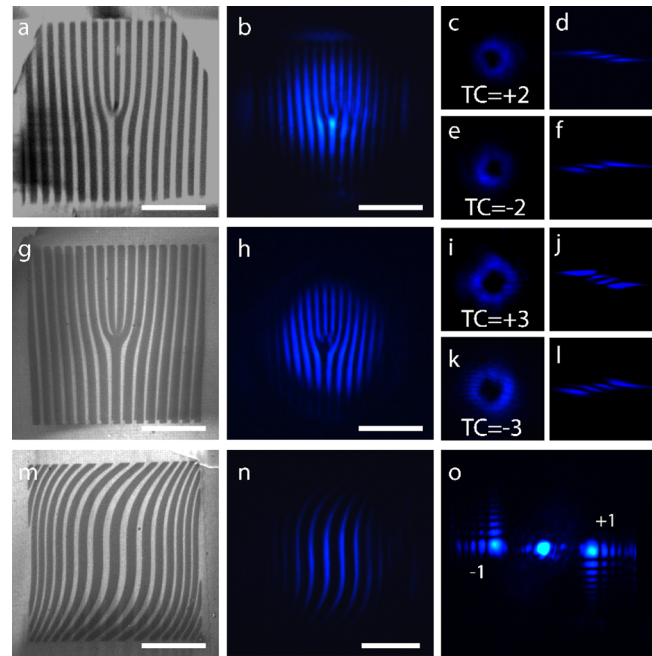
$$\phi(x, y) = \frac{2\pi(x^3 + y^3)}{\rho_c} \tag{5}$$

Figure 4. Generation of SH vortices with TC = 2, 3, and Airy beam. (a) SEM image and (b) SH image of the fabricated CGH on WS$_2$ monolayer for generating SH vortex with TC = ± 2. (c,e) Far-field images of SH vortices in the +1 and −1 diffraction order and (d,f) the corresponding cylindrical lens images indicating the TC of +2 and −2, respectively. (g−l) Experimental results for generating SH vortex with TC = ±3. (m) SEM image of the fabricated CGH with cubic phase modulation on WS$_2$ monolayer for producing the 2D-Airy beam. (n) SH image of the same hologram. (o) Far-field image of SH Airy beams at the ±1 diffraction order. Scale bars are 10 μm.

where ρ_c represents the period of cubic modulation. The amplitude profile is set as $A(x, y) = 1$. Figure 4m,n shows the SEM image and SH image of the fabricated hologram, whereas Figure 4o shows the generated SH Airy beams in the +1 and −1 diffraction order. We verify the accuracy of the nonlinear TMD holograms by fitting the measured optical intensity distributions of all the generated SH vortex beams and Airy beam with theoretically calculated intensity profiles, which are plotted in Figure S6 of Supporting Information (see Supporting Information S3).

Lastly, the reconstruction of complex holographic images is further demonstrated using the nonlinear TMD holograms. The designed binary-amplitude CGH is obtained by performing the discrete Fourier transform of the irregular phase and amplitude information on an image (details in Methods). Figure 5a is the original image, which is the Chinese character for the word "light". Figure 5b is the corresponding computed binary-amplitude CGH with 200 × 200 pixels. The SEM images of the fabricated hologram patterned on WS$_2$ monolayer over an area of 25 × 25 μm^2 is shown in Figure 5d,e. Hence, the pixel size in the patterned hologram is 125 nm.

Figure 5c shows the numerically reconstructed holographic image of the original image formed in the ±1 diffraction order, whereas Figure 5f displays the optically reconstructed SH image from the fabricated hologram at the SHG wavelength of 450 nm. In Figure 5g, the broadband operation functionality of the nonlinear TMD holograms are demonstrated with the SH image reconstruction at three more SHG wavelengths of 415, 500, and 520 nm. The signal-to-noise ratio (SNR) for the
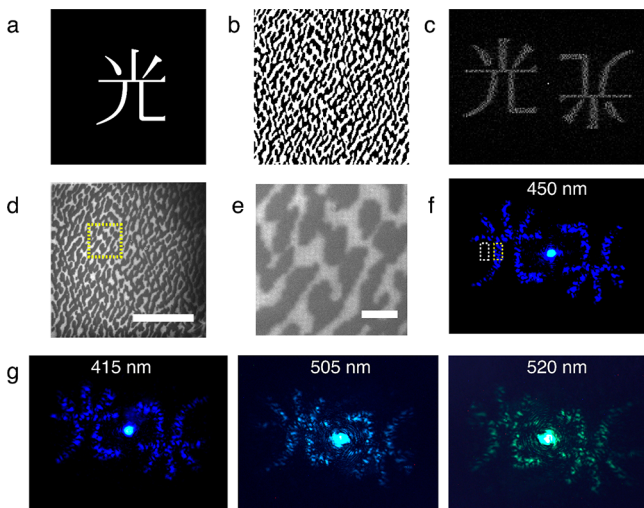
Figure 5. Reconstruction of complex holographic image. (a) Image of the original object which is the Chinese character for the word "light". (b) Calculated binary-amplitude CGH pattern with 200 × 200 pixels, where the dark and bright parts represent 0 and 1 amplitude values, respectively. (c) Numerical reconstruction of the original image formed in the ±1 diffraction order. (d) SEM image of the fabricated hologram on WS$_2$ monolayer in an area of 25 × 25 μm^2 (scale bar is 10 μm) and (e) the zoomed-in view of the yellow dashed square area (scale bar is 1 μm). The dark part indicates the etched-out area during the FIB milling. (f) Optical reconstruction of the original image formed at SH wavelength 450 nm. The area highlighted by the yellow dashed rectangle on the reconstructed image is used for measuring the mean intensity of the image whereas the area highlighted by the white dashed rectangle is used for measuring the mean background noise. (g) Reconstructed holographic images at SH wavelengths at 415, 505, and 520 nm.

reconstructed images can be defined as the ratio between the mean intensity from a particular area of the image and the mean value of the background noise from an adjacent dark area. The SNR can serve as the figure of merit for assessing the quality of the reconstructed image and thereby the quality of the nonlinear TMD hologram. To measure the SNR, we consider the mean intensity of a 40 × 80 pixel area of the image (highlighted by the yellow dashed rectangle in Figure 5f) and the mean background noise from an adjacent dark area of the same size (highlighted by the white dashed rectangle in Figure 5f). The measured SNRs for the images at the SH wavelengths of 415, 450, 500, and 520 nm are 7.94, 7.81, 4.57 and 3.85, respectively. Additionally, the dependence of the SNR on the pixel size of hologram is also characterized in Figure S7 and Table S1 of Supporting Information.

In summary, we have demonstrated the concept of nonlinear TMD holograms with high conversion efficiency and atomic thickness made of only single nanopatterned TMD monolayer for SH beam shaping and holographic image reconstruction. The beam-shaping capability of the hologram is illustrated by the generation of SH vortex beams and 2D-Airy beam. The conversion efficiency of nonlinear TMD holograms is notably higher than the previously reported metasurface holograms. Furthermore, the valley-contrasting physics associated with the TMD monolayer is observed to provide the deterministic control over the output polarization state of the generated SH beam. Not only WS$_2$, but this concept can be employed for other types of TMDs and 2D materials as well. Moreover, TMD monolayers are also known for possessing high third-

order nonlinear susceptibility.[33] Thus, the same TMD holograms can easily be extended to other nonlinear optical processes such as THG, four-wave mixing, sum and difference frequency generation, and so forth. The atomic scale thickness makes these TMD holograms an ideal candidate to be integrated with modern flat optoelectronics and on-chip wavelength multiplexing devices for beam manipulation, optical data storage, optical communications, and information security. Apart from this, the transparent nature with the atomic thickness of the TMD holograms can be harnessed for security cryptograms on banknotes and credit cards.

Methods. *Computer-Generated Hologram.* The binary-amplitude CGH is generated using the Lee method[21] by using the Matlab for the numerical calculation. First a complex field of the hologram $A(x, y)e^{i\phi(x, y)}$ is obtained by taking the Fourier transform of the target image where the amplitude $A(x, y)$ is a positive normalized function and the phase $\phi(x, y)$ is the desired phase pattern having a value within $[-\pi, \pi]$. Following the Lee method by encoding the full phase and amplitude information into a binary-amplitude pattern, the generated hologram $h(x, y) \in \{0,1\}$ can be represented as

$$h(x, y) = \frac{1}{2} + \frac{1}{2}\text{sgn}\left\{\cos\left[\frac{2\pi x}{\Lambda} - \phi(x, y)\right] - \cos[\sin^{-1}(A(x, y))]\right\}$$

(6)

where Λ is the grating period. The value of 0 or 1 for $h(x, y)$ at each pixel in the hologram signifies whether WS$_2$ needs to be etched out or not during the FIB process.

Sample Preparation. The nonlinear TMD holograms are fabricated on single-crystal WS$_2$ monolayer triangles grown by low-pressure chemical vapor deposition on c-cut (0001) sapphire substrate (2D semiconductors). The binary-amplitude CGHs are patterned on the WS$_2$ monolayer by focused ion beam milling (FEI Helios Nanolab 600, Ga$^+$ source, 30 kV, 1.5 pA). The ion dose, milling dwell time, and astigmatism of the ion beam are carefully optimized to ensure the design accuracy and minimize the Ga$^+$ contamination.

Optical Setup. The schematic of the experimental setup used for the optical characterization is illustrated in Figure S1 of Supporting Information. Femtosecond laser pulse at the fundamental wavelength from a tunable Ti:Sapphire oscillator (Coherent Chameleon, wavelength range 690−1040 nm, repetition rate 80 MHz, pulse width <100 fs) is transmitted through a linear polarizer and a quarter-wave plate and then slightly focused on the TMD hologram sample using a 4× objective lens (NA = 0.12). The average fundamental pump power of 80 mW is used corresponding to the pump power density of 21.1 KW·cm^{-2}. SH emission from the hologram sample is collected by either a 20× objective (NA = 0.42) or a 60× objective (NA = 0.8), filtered spectrally to remove the transmitted fundamental pump beam and then imaged either in k-space or real space using a color charge-coupled device (CCD) camera. For the quantification of the SH beam intensity of different diffraction orders, an electron-multiplying CCD (EMCCD, Andor iXon Ultra) is used instead of the color CCD. For polarization state characterization of the SH emission, another combination of a quarter-wave plate and a linear polarizer is inserted before the imaging CCD.

ASSOCIATED CONTENT

Ⓢ Supporting Information

The Supporting Information is available free of charge on the ACS Publications website at DOI: 10.1021/acs.nanolett.9b02740.

> Illustration of the experimental setup, characterization of the wavelength dependence of the diffraction angle for a fork grating, dependence of the diffraction angle on the grating period, vortex helicity measurement with LCP fundamental pump beam, dependence of the parallel and perpendicular components of SH vortices on the linear polarization angle of pump beam, intensity profile measurement for the vortex beams and the 2D-Airy beam, dependence of the signal-to-noise ratio on the pixel size of hologram, and method of the Stokes parameter measurements (PDF)

AUTHOR INFORMATION

Corresponding Authors
*E-mail: (J.G.) gaojie@mst.edu.
*E-mail: (X.Y.) yangxia@mst.edu.

ORCID ⓘ
Jie Gao: 0000-0003-0772-4530
Xiaodong Yang: 0000-0001-9031-3155

Author Contributions

The manuscript was written through contributions of all authors. All authors have given approval to the final version of the manuscript.

Notes

The authors declare no competing financial interest.

ACKNOWLEDGMENTS

REFERENCES

(1) Leith, E. N.; Upatnieks, J. *J. Opt. Soc. Am.* **1962**, *52* (10), 1123–1130.
(2) Dufresne, E. R.; Grier, D. G. *Rev. Sci. Instrum.* **1998**, *69* (5), 1974–1977.
(3) Curtis, J. E.; Koss, B. A.; Grier, D. G. *Opt. Commun.* **2002**, *207* (1–6), 169–175.
(4) Heanue, J. F.; Bashaw, M. C.; Hesselink, L. *Science* **1994**, *265* (5173), 749–752.
(5) Psaltis, D.; Burr, G. W. *Computer* **1998**, *31* (2), 52–60.
(6) Matoba, O.; Nomura, T.; Perez-Cabre, E.; Millan, M. S.; Javidi, B. *Proc. IEEE* **2009**, *97* (6), 1128–1148.
(7) Blanche, P.-A.; Bablumian, A.; Voorakaranam, R.; Christenson, C.; Lin, W.; Gu, T.; Flores, D.; Wang, P.; Hsieh, W.-Y.; Kathaperumal, M.; et al. *Nature* **2010**, *468* (7320), 80.
(8) Shapira, A.; Naor, L.; Arie, A. *Sci. Bull.* **2015**, *60* (16), 1403–1415.
(9) Segal, N.; Keren-Zur, S.; Hendler, N.; Ellenbogen, T. *Nat. Photonics* **2015**, *9* (3), 180.
(10) Ye, W.; Zeuner, F.; Li, X.; Reineke, B.; He, S.; Qiu, C.-W.; Liu, J.; Wang, Y.; Zhang, S.; Zentgraf, T. *Nat. Commun.* **2016**, *7*, 11930.
(11) Keren-Zur, S.; Avayu, O.; Michaeli, L.; Ellenbogen, T. *ACS Photonics* **2016**, *3* (1), 117–123.
(12) Chen, Y.; Yang, X.; Gao, J. *Adv. Opt. Mater.* **2018**, *6* (19), 1800646.
(13) Walter, F.; Li, G.; Meier, C.; Zhang, S.; Zentgraf, T. *Nano Lett.* **2017**, *17* (5), 3171–3175.
(14) Almeida, E.; Bitton, O.; Prior, Y. *Nat. Commun.* **2016**, *7*, 12533.
(15) Li, G.; Chen, S.; Pholchai, N.; Reineke, B.; Wong, P. W. H.; Pun, E. Y. B.; Cheah, K. W.; Zentgraf, T.; Zhang, S. *Nat. Mater.* **2015**, *14* (6), 607.
(16) Almeida, E.; Prior, Y. *Sci. Rep.* **2015**, *5*, 10033.
(17) Gao, Y.; Fan, Y.; Wang, Y.; Yang, W.; Song, Q.; Xiao, S. *Nano Lett.* **2018**, *18* (12), 8054–8061.
(18) Janisch, C.; Wang, Y.; Ma, D.; Mehta, N.; Elías, A. L.; Perea-López, N.; Terrones, M.; Crespi, V.; Liu, Z. *Sci. Rep.* **2015**, *4*, 5530.
(19) Autere, A.; Jussila, H.; Dai, Y.; Wang, Y.; Lipsanen, H.; Sun, Z. *Adv. Mater.* **2018**, *30* (24), 1705963.
(20) Seyler, K. L.; Schaibley, J. R.; Gong, P.; Rivera, P.; Jones, A. M.; Wu, S.; Yan, J.; Mandrus, D. G.; Yao, W.; Xu, X. *Nat. Nanotechnol.* **2015**, *10* (5), 407.
(21) Lee, W.-H. *Appl. Opt.* **1979**, *18* (21), 3661–3669.
(22) Shapira, A.; Juwiler, I.; Arie, A. *Opt. Lett.* **2011**, *36* (15), 3015–3017.
(23) Sheng, Y.; Kong, Q.; Wang, W.; Kalinowski, K.; Krolikowski, W. *J. Phys. B: At., Mol. Opt. Phys.* **2012**, *45* (5), No. 055401.
(24) Paterson, L.; MacDonald, M. P.; Arlt, J.; Sibbett, W.; Bryant, P.; Dholakia, K. *Science* **2001**, *292* (5518), 912–914.
(25) Padgett, M.; Bowman, R. *Nat. Photonics* **2011**, *5* (6), 343.
(26) Nagali, E.; Sansoni, L.; Sciarrino, F.; De Martini, F.; Marrucci, L.; Piccirillo, B.; Karimi, E.; Santamato, E. *Nat. Photonics* **2009**, *3* (12), 720.
(27) Wang, J.; Yang, J.-Y.; Fazal, I. M.; Ahmed, N.; Yan, Y.; Huang, H.; Ren, Y.; Yue, Y.; Dolinar, S.; Tur, M.; et al. *Nat. Photonics* **2012**, *6* (7), 488.
(28) Denisenko, V.; Shvedov, V.; Desyatnikov, A. S.; Neshev, D. N.; Krolikowski, W.; Volyar, A.; Soskin, M.; Kivshar, Y. S. *Opt. Express* **2009**, *17* (26), 23374–23379.
(29) Liu, S.; Sinclair, M. B.; Saravi, S.; Keeler, G. A.; Yang, Y.; Reno, J.; Peake, G. M.; Setzpfandt, F.; Staude, I.; Pertsch, T.; et al. *Nano Lett.* **2016**, *16* (9), 5426–5432.
(30) Gili, V.; Carletti, L.; Locatelli, A.; Rocco, D.; Finazzi, M.; Ghirardini, L.; Favero, I.; Gomez, C.; Lemaître, A.; Celebrano, M.; et al. *Opt. Express.* **2016**, *24* (14), 15965–15971.
(31) Autere, A.; Jussila, H.; Marini, A.; Saavedra, J.; Dai, Y.; Säynätjoki, A.; Karvonen, L.; Yang, H.; Amirsolaimani, B.; Norwood, R. A.; et al. *Phys. Rev. B* **2018**, *98* (11), 115426.
(32) Liu, H.; Li, Y.; You, Y. S.; Ghimire, S.; Heinz, T. F.; Reis, D. A. *Nat. Phys.* **2017**, *13* (3), 262.
(33) Säynätjoki, A.; Karvonen, L.; Rostami, H.; Autere, A.; Mehravar, S.; Lombardo, A.; Norwood, R. A.; Hasan, T.; Peyghambarian, N.; Lipsanen, H.; Kieu, K.; Ferrari, A. C.; Polini, M.; Sun, Z. *Nat. Commun.* **2017**, *8* (1), 893.
(34) Xiao, J.; Ye, Z.; Wang, Y.; Zhu, H.; Wang, Y.; Zhang, X. *Light: Sci. Appl.* **2015**, *4* (12), No. e366.
(35) Baumgartl, J.; Mazilu, M.; Dholakia, K. *Nat. Photonics* **2008**, *2* (11), 675.
(36) Vettenburg, T.; Dalgarno, H. I. C.; Nylk, J.; Coll-Lladó, C.; Ferrier, D. E. K.; Čižmár, T.; Gunn-Moore, F. J.; Dholakia, K. *Nat. Methods* **2014**, *11*, 541.